

# Promoting N–H Bond Formation by an Alkali Metal Hydride under Confinement

Published as part of *Energy & Fuels* virtual special issue “2024 Energy and Fuels Rising Stars”.

Meng Zhu, Haolan Tao,\* Cheng Lian,\* and Honglai Liu



Cite This: *Energy Fuels* 2024, 38, 13444–13454



Read Online

ACCESS |



Metrics & More

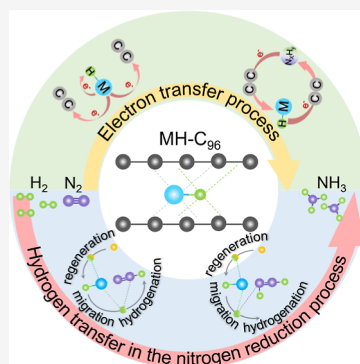


Article Recommendations



Supporting Information

**ABSTRACT:** The activation of dinitrogen is the key step in ammonia production, which is usually conducted at transition-metal catalysts (Fe and Ru) with the condition of high temperatures and pressures (400–500 °C and 10–30 MPa). A recent development in catalytic ammonia synthesis is the use of potassium hydride-intercalated graphite ( $K_xH_yC_z$ ) as catalysts, which can activate dinitrogen at relatively moderate temperatures and pressures (250–400 °C and 1 MPa) without expensive transition metals. The nanoconfinement of alkali metal hydride between the graphene layers plays an important role in the activation and conversion of dinitrogen. It is attractive to further elucidate the interplay rules between nitrogen-based intermediates, metal hydride, and graphene layers. In this work, we designed three kinds of alkali metal hydride (MH)-intercalated graphene catalysts ( $Li_xHC_{96}$ ,  $Na_xHC_{96}$ ,  $K_xHC_{96}$ ) as a platform for exploring the reaction mechanism of nitrogen at two-dimensional confinement. We found that the alternating associative pathway of the ammonia synthesis is dominant over the MH-intercalated graphene catalysts. The activated  $*H$  from MH contributes to the hydrogenation process of  $N_2$  to form  $NH_3$  molecules. The graphene layers with Å-level confined spacing promote the electron transfer between the reaction intermediate and alkali metals, which is favorable for the regeneration of the  $MHC_{96}$  catalytic system. This work provides theoretical insights into the design of alkali metal hydride-based catalysts for nitrogen activation.



## 1. INTRODUCTION

Ammonia is not only an important chemical for producing fertilizers, dyes, explosives, and resins<sup>1</sup> but also a potential hydrogen carrier, effectively addressing the challenges associated with hydrogen energy storage and transportation.<sup>2</sup> The Haber–Bosch process is commonly used for the industrial synthesis of ammonia ( $N_2 + 3H_2 \rightarrow 2NH_3$ ) under high temperature and pressure conditions (400–500 °C and 10–30 MPa), which requires the use of transition-metal catalysts such as iron (Fe) or ruthenium (Ru).<sup>3</sup> The ammonia synthesis process in industry accounts for more than 1% of global energy consumption with serious greenhouse gas emission.<sup>4</sup> To reduce energy consumption and  $CO_2$  emission, it is significant to explore potential catalysts that can work under milder temperatures and pressures for the thermal catalytic conversion of nitrogen.

During traditional ammonia synthesis processes,  $N_2$  is adsorbed and dissociated directly on transition-metal catalysts, and the free N is hydrogenated to produce  $NH_3$ .<sup>5</sup> The rate-determining step is the breaking of the stable  $N\equiv N$  bond (945  $kJ\ mol^{-1}$ ), and there also exists a competitive relationship between nitrogen adsorption and product desorption, which can be broken by modifying the electronic state of transition metals with additional active centers.<sup>6</sup> Chang et al. achieved the thermal catalytic conversion of nitrogen under the conditions of 300–400 °C and 1 MPa by utilizing transition-

metal nitrides and alkali metal hydrides ( $Mn_4N-AHs$ ).<sup>7</sup> The alkali metal hydrides acted as the second active center, capturing free nitrogen on the transition metal and facilitating the hydrogenation of nitrogen. Wang et al. also proposed the use of LiH as the second active center for nitrogen hydrogenation and subsequent ammonia formation, reducing the reliance on the transition metal.<sup>8</sup> Guan et al. proved that the hydridic hydrogen acts as an electron donor and facilitates the activation of  $N_2$  with concurrent  $H_2$  release by studying the function of hydrogen vacancies created at the  $BaH_2$  surface, which can adsorb and activate  $N_2$ .<sup>9</sup> Cao et al. investigated the associative mechanism of the thermo-catalytic ammonia synthesis system in  $Ca_3CrN_3H$  with the active centers of arranged  $Ca_3$  holes modified electronically by a distant Cr, finding that dilution of the surface active site helped to strengthen the association mechanism due to the inherent structure.<sup>10</sup> Wu et al. utilized NaH as a mediator to achieve the hydrogenation of fixed N to  $NH_3$  under ambient temperature

Received: March 6, 2024

Revised: June 26, 2024

Accepted: June 27, 2024

Published: July 8, 2024



and avoid the plasma-induced ammonia cracking in the plasma-driven chemical looping ammonia synthesis process (PCLAS loop).<sup>11</sup> Accordingly, compared to conventional transition-metal catalysts, the addition of electron-promoting alkali (earth) metal hydrides (LiH, NaH, KH, BaH<sub>2</sub>) can enhance the catalytic activity of ammonia synthesis by 2–4 orders of magnitude<sup>12</sup> and reduce the requirements of the reaction conditions.<sup>13</sup> Chen et al. found that K promoter can facilitate the adsorption of N<sub>2</sub> at the coordination of unsaturated iron sites in the cyclopentadienylidene form.<sup>14</sup> Besides, Kalucki and Morawski used iron intercalated in graphite as catalysts for ammonia synthesis; the iron coordinated by carbon and potassium can influence the intensity of the electron paramagnetic resonance signal and activity.<sup>15</sup> For electrochemical ammonia synthesis, Noskov et al. found that lithium-mediated nitrogen reduction reaction (Li-NRR) in nonaqueous electrolytes can efficiently produce ammonia from N<sub>2</sub>.<sup>16</sup> Their study focused on optimizing the Li-NRR process through multiple strategies that includes potential cycling,<sup>17</sup> using oxygen as a promoter,<sup>18</sup> employing potential proton shuttles,<sup>19,20</sup> increasing electrode surface area,<sup>21,22</sup> regulating electrolyte interfaces,<sup>23</sup> and designing a continuous-flow electrolyzer with gas diffusion electrodes.<sup>24</sup> They also explored advanced materials to improve the efficiency and scalability of electrochemical ammonia synthesis, such as the new electrolyte of calcium tetrakis-(hexafluoroisopropoxy)borate for calcium-mediated NH<sub>3</sub> synthesis.<sup>25</sup> Totally, it is worth noting that the use of alkali metal hydrides has the potential to reduce the need for expensive transition-metal catalysts and even serve as a replacement.

Nanoconfinement is expected to enhance the reversible hydrogen storage capability<sup>26</sup> and catalytic activity of metal hydrides.<sup>27–29</sup> Graphene, a two-dimensional carbon material with exceptional electronic, mechanical, and thermal properties, possesses a large surface area that prevents hydrogen molecule aggregation, making it an effective supporting material for metal hydrides.<sup>30,31</sup> Intercalating the metal hydrides into graphene can modify the electronic,<sup>32</sup> magnetism,<sup>33</sup> and vibration<sup>34</sup> properties of the two-dimensional confined system.<sup>35,36</sup> Ahmad et al. studied the alkali metal halide-intercalated graphene theoretically, finding that the van der Waals interaction between alkali metals and halogens disrupts the electron pairing (M<sup>+</sup>–C<sup>-</sup>) within alkali metals and graphene layers and subsequently results in the charge transfer shifting from the alkali metal–graphene to the alkali metal–halogen.<sup>37</sup> Therefore, the intercalation of halogen atoms can control the charge transfer between alkali metals and graphene bilayers. Shi et al. have successfully synthesized highly dispersed tungsten carbide nanoparticles (NPs) sandwiched between few-layer reduced graphene oxide (RGO), reducing the requirement of Pt for the same performance by the intercalated structure and synergistic effect.<sup>38</sup> Kikuchi et al. found that the lamellar compound of graphite (LCG) intercalated by ferric chloride can catalyze the synthesis of hydrocarbons with outstandingly high selectivity (more than 90% at 400 °C).<sup>39</sup> Moreover, the embedded alkali metals in the graphene layers exhibit metallic characteristics, and the energetic positions of the interlayer states can be controlled by intercalating different metal atoms, inducing phonon-mediated superconductivity.<sup>40,41</sup> Chang et al. prepared a KH-intercalated graphite catalyst (KH<sub>0.19</sub>C<sub>2.4</sub>) for the catalytic ammonia synthesis.<sup>42</sup> With the introduction of N<sub>2</sub> and H<sub>2</sub> by a 1:3

ratio to a fixed-bed reactor under milder operating conditions, the ammonia productivity was comparable to that of the traditional transition-metal catalyst Ru/MgO at temperatures of 250–400 °C and 1 MPa. Therefore, since the alkali metal hydride nanoconfined between the graphene layers can contribute to the activation and conversion of dinitrogen, it is important to further discuss the effect of the identity of alkali metal hydrides on the catalytic mechanism and the interplay picture between nitrogen-based intermediates, alkali metal hydrides, and graphene layers during the nitrogen reduction reaction (NRR) process.

In this work, we designed three MH-intercalated graphene (LiHC<sub>96</sub>, NaHC<sub>96</sub>, KHC<sub>96</sub>) catalysts to study the NRR process at nanoconfinement using density functional theory (DFT) calculations. We first evaluated the distal and alternative reaction pathways of the ammonia synthesis over the MH-intercalated graphene catalysts. The analysis of the orbital and charge properties was performed to reveal the electronic interplay between nitrogen-based intermediates, alkali metal hydride, and graphene layers. Finally, we presented a detailed illustration of the activation and hydrogenation mechanisms of dinitrogen over the MH-intercalated graphene catalysts.

## 2. COMPUTATIONAL DETAILS

**2.1. DFT Calculations.** The energy and charge properties of the MH-intercalated graphene systems are calculated using the Vienna ab initio simulation Package<sup>43–45</sup> and choosing the Perdew–Burke–Ernzerhof exchange–correlation functional.<sup>46</sup> The electron–ion interaction in the system is described using the projector-augmented wave method<sup>47</sup> and the cutoff energy for the plane-wave basis was 420 eV. For different MH-intercalated graphene catalysts, a Monkhorst–Pack *k*-point mesh with a 2 × 2 × 1 *k*-point grid is used to sample the Brillouin zone. The DFT-D3 correction method was employed to illustrate the long-range dispersion interactions between the adsorbates and catalysts.<sup>48</sup> In all models for calculation, a vacuum layer of 10 Å was added to the *z*-direction to avoid the effect of adjacent periodic structures on the calculation results. With the energy convergence criteria of 10<sup>-5</sup> eV and the force convergence criteria of 0.02 eV/Å, the structures of the MH-intercalated graphene catalysts and subsequent nitrogen-based intermediates were fully optimized. The intercalation energy ( $\Delta E^{\text{Int}}$ ) and relative energy ( $\Delta E^{\text{Rxn}}$ ) were calculated as

$$\Delta E^{\text{Int}} = E_{\text{M}_x\text{HC}_{96}} - \left( E_{\text{C}_{96}} + xE_{\text{M}} + \frac{1}{2}E_{\text{H}_2} \right) \quad (1)$$

$$\Delta E^{\text{Rxn}} = E_{\text{M}_x\text{HC}_{96}\text{-N}_2\text{H}_y} - \left( E_{\text{M}_x\text{HC}_{96}} + E_{\text{N}_2} + \frac{y}{2}E_{\text{H}_2} \right) \quad (2)$$

where  $E_{\text{M}_x\text{HC}_{96}}$ ,  $E_{\text{C}_{96}}$ ,  $E_{\text{M}}$ , and  $E_{\text{H}_2}$  represent total energies of the MH-intercalated graphene, graphene, alkali metal atoms, and hydrogen molecules.  $E_{\text{M}_x\text{HC}_{96}\text{-N}_2\text{H}_y}$  is the energy of the catalyst binding intermediates (N<sub>2</sub>H<sub>y</sub>),  $E_{\text{M}_x\text{HC}_{96}}$  and  $E_{\text{N}_2}$  are the energy of the catalyst and N<sub>2</sub> molecule, and  $y/2E_{\text{H}_2}$  represents the energy of the H<sub>2</sub> molecule required for the reduction reaction.

**2.2. Reaction Mechanism.** Previous studies reported that the NRR pathway on MH-intercalated graphene catalysts is more favorable for the associative pathway, bypassing the strong energy barrier of direct nitrogen dissociation before hydrogenation.<sup>42,49,50</sup> In the associative mechanism, N<sub>2</sub> is adsorbed on alkali metals but cannot directly dissociate in the

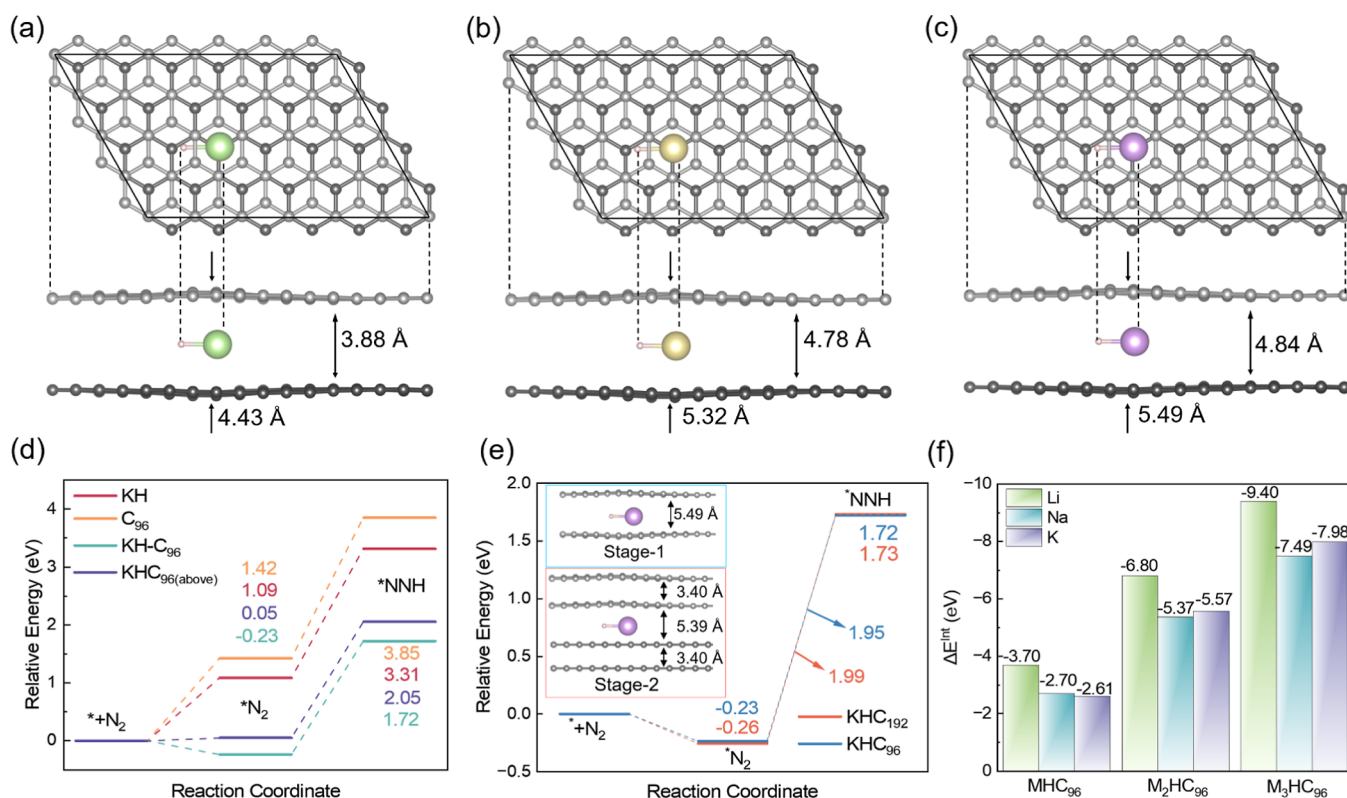


**Figure 1.** Top and side views of optimized catalyst structures. Structure model of (a) LiH-intercalated graphene ( $\text{LiHC}_{96}$ ), (b) NaH-intercalated graphene ( $\text{NaHC}_{96}$ ), and (c) KH-intercalated graphene ( $\text{KHC}_{96}$ ). (d) Relative energy diagram for  $\text{N}_2$  adsorption and the first hydrogenation step on the KH, graphene interlayer,  $\text{KHC}_{96}$ , and  $\text{KHC}_{96(\text{above})}$ . (e) Alkali metal hydride-intercalated graphene (stage-1) and four-layer graphite slabs (stage-2). (f) Intercalation energy of  $\text{M}_x\text{H}$ -intercalated graphene (M: Li, Na, K). The green, yellow, purple, white, and gray atoms represent lithium (Li), sodium (Na), potassium (K), hydrogen (H), and graphene, respectively.

interlayer of the catalyst. Instead, the activated H attacks the  $\text{N}_2$ , leading to the complete cleavage of the  $\text{N}\equiv\text{N}$  bond and the formation of the ammonia molecules. This study investigates the NRR process on different MH-intercalated graphene catalysts using the distal associative pathway and alternating associative pathway (Figure S1). In the distal associative pathway, the distal N is preferentially reduced to produce ammonia, and the proximal N is then hydrogenated to produce a second ammonia. However, in the alternating associative pathway, H reacts with two N in turn until N is completely reacted. By calculating the relative energy changes of reaction intermediates, the reaction pathways during the NRR process can be analyzed in different catalytic systems.

**2.3. Model Description.** In the previous experimental research, the hydrogen content quantification result shows that  $\sim 24\%$  hydrogen remained in the catalyst after the intercalation process, which provides a molar ratio of 4:1 for K/H in the catalyst.<sup>42</sup> In addition, ICP elemental analysis shows that the stoichiometry of K/C in the catalyst is 1:24. Therefore, we choose the ratio of the C atom to the hydrogen atom to be 96:1 in our model and study the effect of different alkali metal numbers and species on the NRR process. As shown in Figure 1a–c, in the MH-intercalated graphene catalysts named  $\text{MHC}_{96}$  (M = Li, Na, K), the alkali metal hydride was supported at the interlayer spacing between the graphene layers with the supercell of  $6 \times 4 \times 1$ , containing 48C atoms in each graphene layer. The interlayer spacing of the initial graphene bilayer model is 5 Å, and the structure is optimized after insertion of the alkali metal hydride. The distance between the layers of graphene is proportional to the diameter

of the alkali metal atoms, with optimized interlayer distances of 4.43 Å ( $\text{LiHC}_{96}$ ), 5.32 Å ( $\text{NaHC}_{96}$ ), and 5.49 Å ( $\text{KHC}_{96}$ ), respectively. The graphene structure near the alkali metal hydride is slightly deformed, and the interlayer spacing is larger than the distance between the edge graphene layers. In Figure 1d, the  $\text{N}_2$  adsorption energy is  $-0.23$  eV on  $\text{C}_{96}\text{KH}$ , which on pure KH is 1.09 eV and on two adjacent graphene layers (without alkali metal hydride) is 1.42 eV, indicating the enhanced ability of  $\text{N}_2$  adsorption and activation in the MH-intercalated system. The difference of the  $\text{N}_2$  adsorption energy indicates that the adsorption of  $\text{N}_2$  is enhanced by the presence of intercalated KH, which is consistent with the experimental finding that potassium hydride under confinement can activate  $\text{N}_2$ .<sup>42</sup> Considering the situation of KH above the graphene layer, the energy of  $\text{N}_2$  adsorption is 0.05 eV, indicating that the interaction between  $\text{N}_2$  and  $\text{KHC}_{96(\text{above})}$  is weaker than  $\text{KH}-\text{C}_{96}$ . The energy barrier of  $\text{N}_2$  to  $\text{N}^*\text{NH}$  on  $\text{KHC}_{96}$  is 1.95 eV, which is lower than 2.00 eV on  $\text{KHC}_{96(\text{above})}$ , suggesting the positive role of nanoconfinement. The computational conclusion on the effect of nanoconfinement is in line with the previous experiments, which showed that  $\text{CaH}_2$  has no catalytic activity but can catalyze ammonia synthesis under confinement.<sup>10,51</sup> Meanwhile, the effect of the number of graphene layers on the catalyst performance was studied, and the alkali metal hydride was intercalated into the two-layer graphene (stage-1) and four-layer graphite (stage-2) structures, respectively (Figure 1e). The optimized interlayer spacing in the stage-1 model is 5.49 Å. By contrast, the optimized interlayer spacing with the alkali metal hydride in the stage-2 model is 5.39 Å. Moreover, it is also found that the

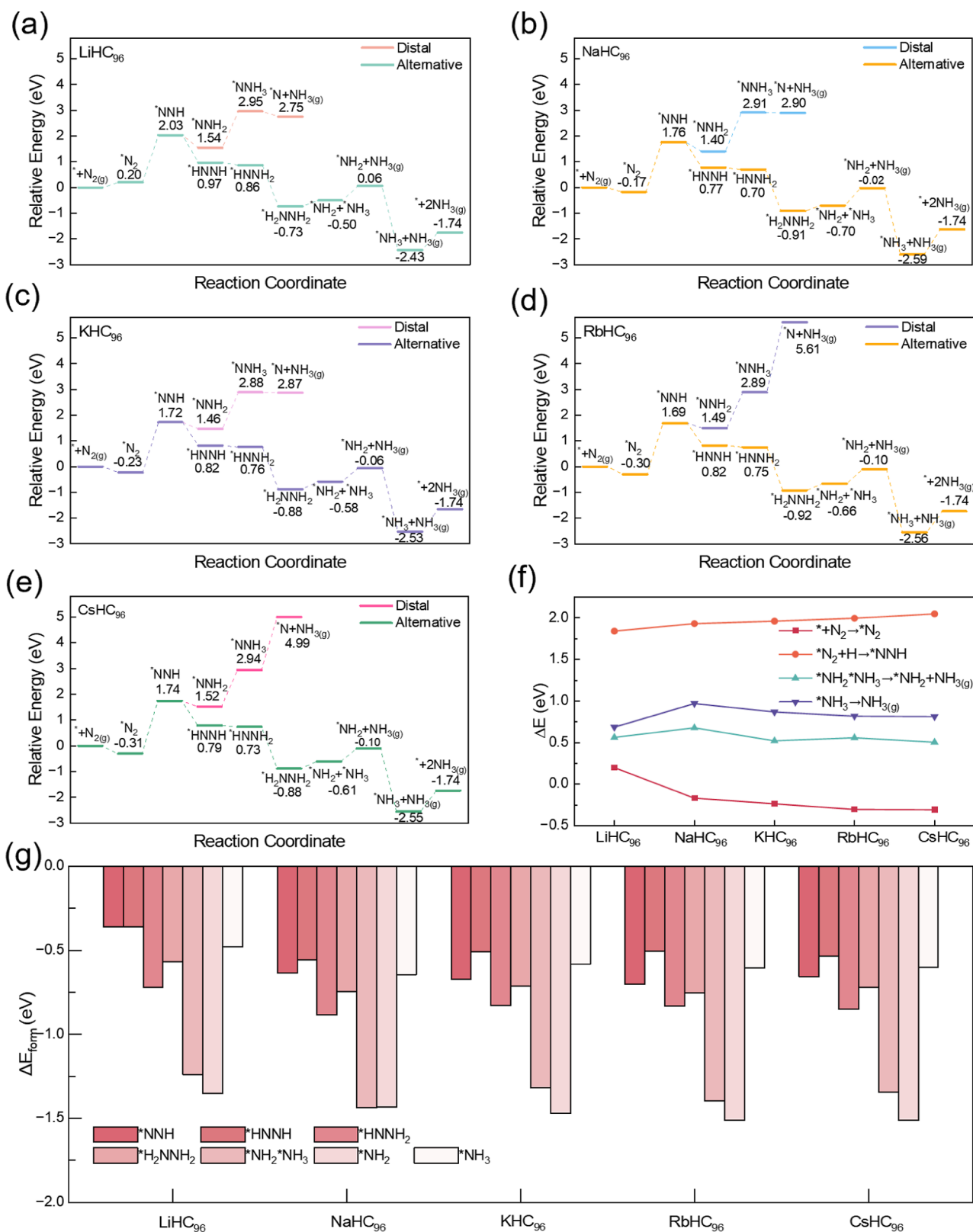


**Figure 2.** Relative energy diagram for distal and alternative pathways of NRR on the catalysts of MHC<sub>96</sub> [(a) LiHC<sub>96</sub>; (b) NaHC<sub>96</sub>; (c) KHC<sub>96</sub>; (d) RbHC<sub>96</sub>; (e) CsHC<sub>96</sub>]. (f) Energy barrier of key steps under an alternating associative pathway on MHC<sub>96</sub> (M = Li, Na, K, Rb, and Cs). (g) Formation energy of NRR intermediates in the alternating associative pathway on MHC<sub>96</sub> catalysts.

energy barriers of the N<sub>2</sub> adsorption and the first hydrogenation step between the two structures were similar. Therefore, the MH-intercalated graphene model (stage-1) is chosen for subsequent calculation, which is more favorable for

the analysis and research of catalytic mechanisms. The intercalation energies of different alkali metal hydrides into the interlayer spacing of the graphene layers in Figure 2f are lower than zero, indicating that these structures are

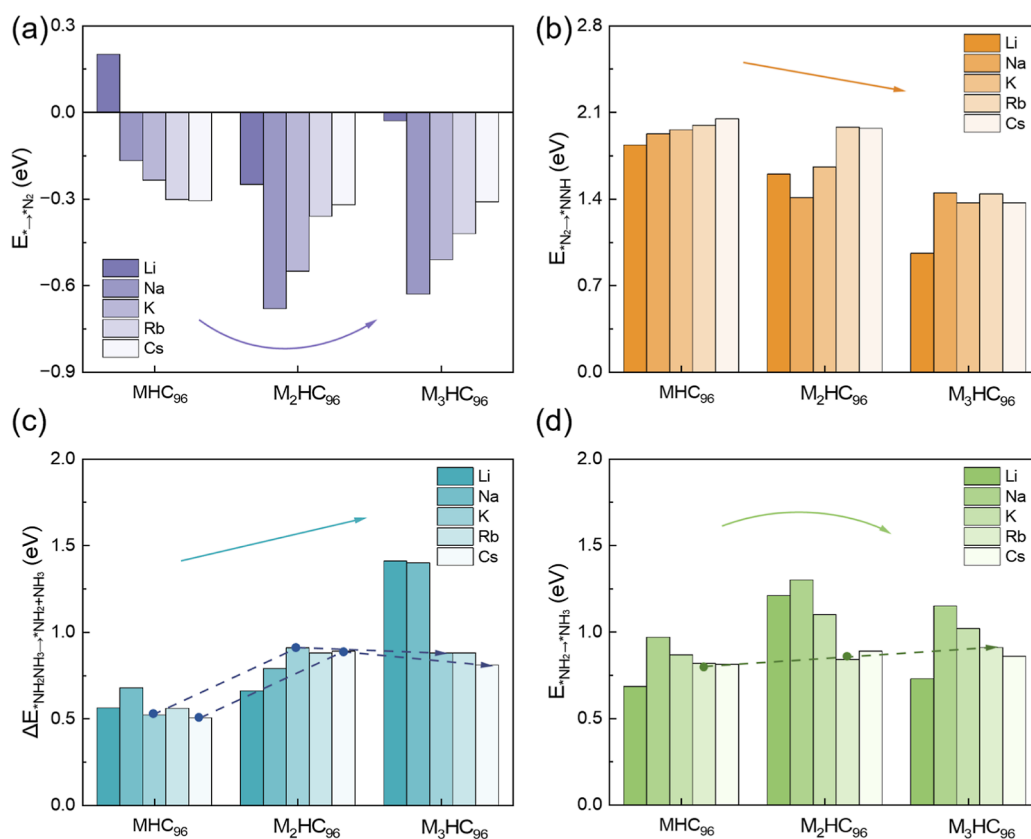


**Figure 3.** (a) Adsorption energy of  $N_2$ , the energy barrier of (b) the first hydrogenation step, (c) formation of the first free ammonia, and (d) the product of the second free ammonia on  $M_xHC_{96}$  ( $x = 1, 2,$  and  $3$ ).

thermodynamically stable. With the increase of the number of alkali metal atoms, the intercalation energy of these catalysts becomes more negative, suggesting that the intercalation structure is easier to form.

### 3. RESULTS

**3.1. Reaction Pathways in  $M_xHC_{96}$  Catalysts.** The nitrogen adsorption and activation on MH-intercalated graphene catalysts observed in previous experiments provide the basis for the mechanism research in our work. For example, Ertl and Thiele had studied the atomic nitrogen surface species on industrial Fe ammonia catalysts by means of X-ray photoelectron spectroscopy (XPS), identifying the N 1s peak at  $\sim 400$  eV on Fe as adsorbed  $N_2$  or  $NH_3$  species.<sup>52</sup> When  $N_2$  is adsorbed on an MH-intercalated graphene catalyst of  $KH_{0.19}C_{24}$ , a broad N 1s peak was also observed at 399.2 eV by XPS, confirming that dinitrogen could be activated on the surface of the  $KH_{0.19}C_{24}$  catalyst.<sup>42</sup> The energy barrier profiles with the evolution of reaction intermediates in both distal and alternating associative pathways on  $MH_xC_{96}$  catalysts are presented in Figure 2, and the optimized geometries are shown in Figure S2. On  $LiHC_{96}$  (Figure 2a), the adsorption energy of  $N_2$  is 0.20 eV, indicating that  $N_2$  cannot be spontaneously adsorbed on the catalyst. Due to the strong bond energy of  $N\equiv N$ , the first hydrogenation step shows a high energy barrier of 1.83 eV. As the hydrogenation process proceeds, the distal pathway shows higher energy barriers from  $*NNH$  to  $*NNH_2$  ( $-0.49$  eV) and  $*NNH_3$  (1.41 eV) than that from  $*NNH$  to  $*NHNH$  ( $-1.06$  eV) and  $*NHNH_2$  (0.09 eV) in the alternating pathway. On  $NaHC_{96}$  (Figure 2b), the adsorption energy of  $N_2$  is  $-0.17$  eV, indicating that  $N_2$  can spontaneously

adsorb on  $NaHC_{96}$ , which is different from that on  $LiHC_{96}$ . However, compared to the rate-determining step on  $LiHC_{96}$ , it is relatively difficult for the rate-determining step on  $NaHC_{96}$  to occur with an energy barrier of 1.93 eV. The adsorption energy of  $N_2$  on  $KHC_{96}$  is  $-0.23$  eV (Figure 2c), which is smaller than the adsorption energy of  $N_2$  on  $LiHC_{96}$  and  $NaHC_{96}$ , making  $N_2$  adsorption easier. The reaction barrier of  $N_2$  hydrogenation to  $*NNH$  on  $KHC_{96}$  is 1.95 eV, slightly higher than the energy barrier of the rate-determining step on  $NaHC_{96}$ . The energy barrier of the first hydrogenation on  $RbHC_{96}$  and  $CsHC_{96}$  is 1.99 and 2.05 eV (Figure 2d,e), indicating that the formation of the first N–H bond is more difficult. The energy barriers of key steps under alternating associative pathway on  $MHC_{96}$  are plotted in Figure 2f, indicating that the first hydrogenation step is the rate-determining step for the alternating pathway. With the increase of the radius of the alkali metal atom (Li, Na, K, Rb, Cs), the interlayer spacing increases, reducing the confinement formed by graphene layers, which slightly increases the energy barrier of the rate-determining step but decreases the adsorption energy of  $N_2$ . Meanwhile, the formation energy of reaction intermediates ( $N_xH_y$ ) on  $MHC_{96}$  in the alternating associative pathway is further provided in Figure 2g, indicating that these structures are stable to participate in further NRR (Figure S3). Experimental studies have shown that  $N_2$  activation can occur on alkaline earth metal centers (such as  $Ba_2RuH_6$ <sup>53</sup> and a low-valent Ca complex<sup>54</sup>). Therefore, we also consider the alkaline earth elements Mg-, Ca-, and Ba-based materials in the second main group and find that the catalytic NRR also follows the same electron transfer rule on  $MH_2C_{96}$  under confinement (Figures S4–S6). The energy barrier of the first hydrogenation

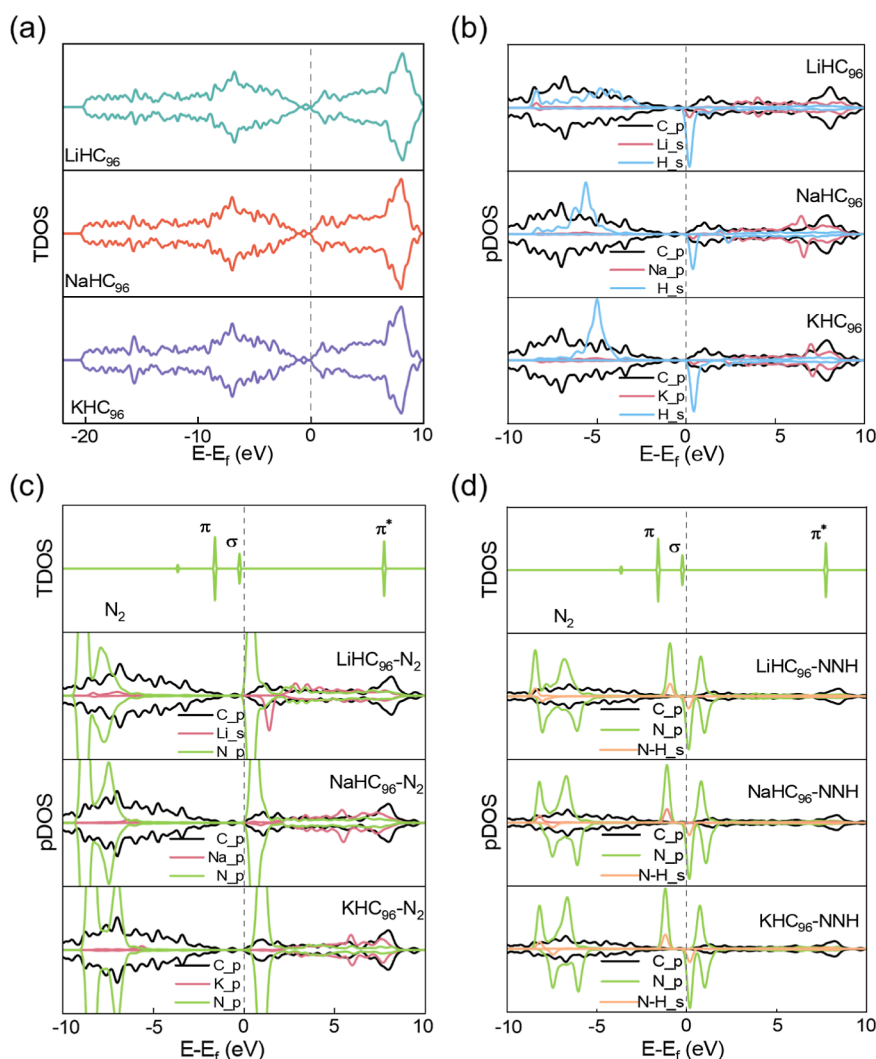


**Figure 4.** (a) TDOS of  $\text{LiHC}_{96}$ ,  $\text{NaHC}_{96}$ , and  $\text{KHC}_{96}$ . (b) PDOS of  $\text{LiHC}_{96}$ ,  $\text{NaHC}_{96}$ , and  $\text{KHC}_{96}$ . (c) DOS of the  $\text{N}_2$  molecule and PDOS of  $\text{LiHC}_{96}$ ,  $\text{NaHC}_{96}$ , and  $\text{KHC}_{96}$  after  $\text{N}_2$  adsorption. (d) TDOS of the  $\text{N}_2$  molecule and PDOS of  $\text{LiHC}_{96}$ ,  $\text{NaHC}_{96}$ , and  $\text{KHC}_{96}$  after the first hydrogenation step.

step is 1.89 eV ( $\text{MgH}_2\text{C}_{96}$ ), 1.83 eV ( $\text{CaH}_2\text{C}_{96}$ ), 1.86 eV ( $\text{BaH}_2\text{C}_{96}$ ), which is lower than 1.95 eV ( $\text{KHC}_{96}$ ), 1.99 eV ( $\text{RbHC}_{96}$ ), 2.05 eV ( $\text{CsHC}_{96}$ ), indicating that the performance of alkali metal hydride as the mediator for NRR is inferior to that of alkali earth metal hydride.

Furthermore, the effect of the content of alkali metal atoms in the interlayer spacing is investigated (Figure S7). It is found in Figure 3a that with the number of alkali metal atoms ranging from 1 to 3, the adsorption energy of  $\text{N}_2$  initially decreases before increasing, indicating a stronger interaction between  $\text{M}_x\text{HC}_{96}$  and  $\text{N}_2$ . The adsorption energy of  $\text{N}_2$  on  $\text{Li}_x\text{HC}_{96}$  is higher than that on  $\text{Na}_x\text{HC}_{96}$ ,  $\text{K}_x\text{HC}_{96}$ ,  $\text{Rb}_x\text{HC}_{96}$ , and  $\text{Cs}_x\text{HC}_{96}$ , indicating that  $\text{N}_2$  adsorption on  $\text{Li}_x\text{HC}_{96}$  is more difficult. In addition, for these  $\text{M}_x\text{HC}_{96}$  catalysts, the energy barriers of the rate-determining step are decreased with increasing the number of alkali metal atoms (Figure 4b). It indicates that the first hydrogenation becomes more favorable as the number of alkali metals increases. On the other hand, the barrier for the desorption of the first free ammonia gradually increases, signifying heightened difficulty in N–N cleavage and desorption (Figure 3c). Finally, the barrier for the desorption of the second free ammonia first decreases and then

increases, which needs to overcome the interaction between M–N bonds (Figure 3d). By analyzing  $\text{N}_2$  adsorption energy and the energy barrier of the NRR steps on  $\text{M}_x\text{HC}_{96}$  ( $x = 1, 2, 3$ ), the catalytic performance is the best on  $\text{M}_3\text{HC}_{96}$ . Although the energy barrier of the rate-determining step on  $\text{Li}_x\text{HC}_{96}$  is lower than that of other  $\text{M}_x\text{HC}_{96}$ , the interaction between  $\text{Li}_x\text{HC}_{96}$  and  $\text{N}_2$  is weaker, making it difficult for the  $\text{N}_2$  adsorption on the  $\text{Li}_x\text{HC}_{96}$  catalyst. Moreover, the energy barrier of the first free ammonia on  $\text{Li}_3\text{HC}_{96}$  and  $\text{Na}_3\text{HC}_{96}$  is higher than other  $\text{MHC}_{96}$ , indicating that the desorption of product ammonia is more difficult. The different trends of the energy barriers of the key reaction steps indicates that the number of alkali metal atoms can affect the catalyst structures and the adsorption configuration of the reaction intermediates, and for simplification, the  $\text{MHC}_{96}$  catalysts are selected for the following analysis of reaction mechanisms. It is worth noting that although the NRR on  $\text{M}_x\text{HC}_{96}$  ( $x \leq 3$ ) is considered to follow the alternating associative mechanism, more complex interactions between alkali metal, graphene, and reaction intermediates can appear at higher content of alkali metal atoms, such as the existence of side adsorption in the reaction process, which may induce different reaction mechanisms.

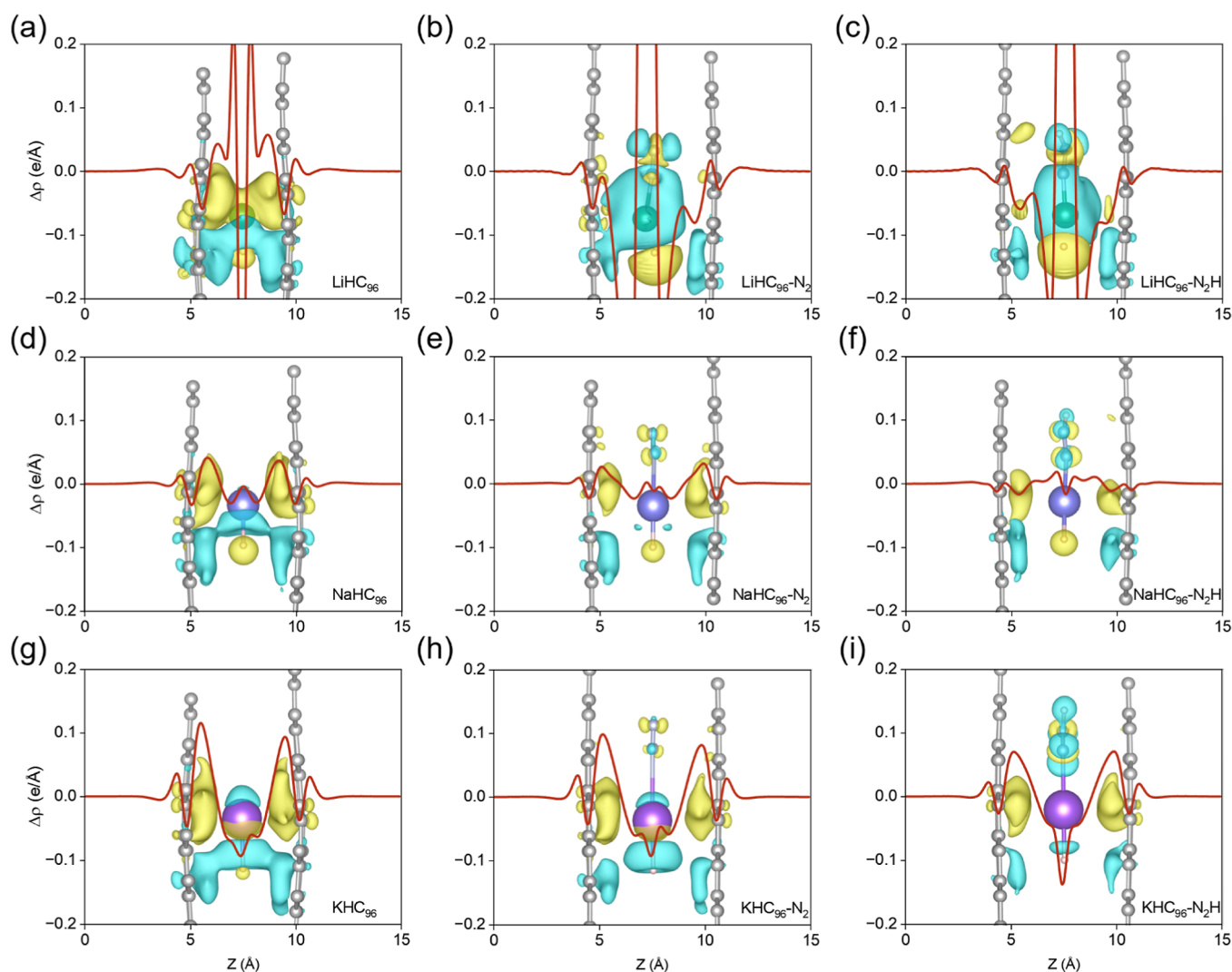


**Figure 5.** Differential charge density for the  $\text{MHC}_{96}$  catalysts before  $\text{N}_2$  adsorption [(a)  $\text{LiHC}_{96}$ ; (d)  $\text{NaHC}_{96}$ ; (g)  $\text{KHC}_{96}$ ], the  $\text{MHC}_{96}$  catalysts after  $\text{N}_2$  adsorption [(b)  $\text{LiHC}_{96}\text{N}_2$ ; (e)  $\text{NaHC}_{96}\text{N}_2$ ; (h)  $\text{KHC}_{96}\text{N}_2$ ], and the  $\text{MHC}_{96}$  catalysts with the  $^*\text{N}_2\text{H}$  intermediate [(c)  $\text{LiHC}_{96}\text{N}_2\text{H}$ ; (f)  $\text{NaHC}_{96}\text{N}_2\text{H}$ ; (i)  $\text{KHC}_{96}\text{N}_2\text{H}$ ], and the overall differential charge density along the  $z$ -axis (red line). The iso-surface value is  $0.0009 \text{ e/Bohr}^3$ . The blue region represents the loss of electrons, and the yellow region represents the gain of electrons.

**3.2. Interaction between  $\text{N}_2$  and  $\text{MHC}_{96}$  Catalysts.** The total density of states (TDOS) of  $\text{N}_2$  and the partial density of states (PDOS) of catalysts and reaction intermediates are shown in Figures 4 and S8–S12. The negative side of the Fermi level ( $E - E_f < 0 \text{ eV}$ ) corresponds to bonding orbitals, while the positive side ( $E - E_f > 0 \text{ eV}$ ) corresponds to antibonding orbitals. The formation of weak van der Waals bonds does not lead to visible changes in the electronic structure of  $\text{MHC}_{96}$  (Figure 4a). For the  $\text{MHC}_{96}$  catalysts, the orbitals of the alkali metal (Li, Na, K) and H overlap near the Fermi level (Figure 4b), indicating the existence of alkali metal hydrides (MH). Differently, the  $s$  orbital of the H atom in the  $\text{LiHC}_{96}$  is distributed more uniformly on the negative side without localized peaks, having strong delocalization of electrons. When moving on to  $\text{NaHC}_{96}$  and  $\text{KHC}_{96}$ , the H atom shows a higher peak in the  $s$  orbital on the negative side of the Fermi level, having relatively localized electrons. The orbitals of alkali metal and graphene-C overlap at the antibonding orbitals, while the orbitals of H and graphene-C orbitals overlap at the bonding orbitals, allowing the electron transfer between alkali metal hydrides and the graphene layers.

As  $\text{N}_2$  adsorbed on  $\text{MHC}_{96}$  (Figure 4c), we find a dispersion of the peaks ( $\sigma$ ,  $\pi$ , and  $\pi^*$ ) of  $\text{N}_2$  orbitals and a decrease of the orbital energy, and an overlap of the orbitals of  $\text{N}_2$ , alkali metal, and graphene-C atom, which determines the interaction between  $\text{N}_2$  and  $\text{MHC}_{96}$ . The higher overlap between the orbitals of  $\text{N}_2$  and graphene-C on  $\text{KHC}_{96}$  suggests a stronger interaction, leading to more stable adsorption of  $\text{N}_2$  on  $\text{KHC}_{96}$ . The distance between the bonding orbitals and the Fermi level shows a sequence of  $\text{LiHC}_{96} > \text{NaHC}_{96} > \text{KHC}_{96}$ , the electron filling probability in  $\text{KHC}_{96}$  at the bonding orbitals higher, making  $\text{N}_2$  more easily adsorbed, and that between the antibonding orbitals and the Fermi level shows a sequence of  $\text{LiHC}_{96} < \text{NaHC}_{96} < \text{KHC}_{96}$ , the electron filling probability in  $\text{KHC}_{96}$  at the antibonding orbitals lower, making  $\text{N}_2$  harder to hydrogenate. In Figure 4d, the dispersion of the  $\text{N}_2$  orbital shows that the interaction between N atoms and catalysts is enhanced. Moreover, the  $\pi^*$  antibonding orbital of the  $\text{N}_2$  molecular orbital hybridizes with the  $s$  orbital of the  $^*\text{H}$  to form a delocalized band that extends below the Fermi level and a new bonding orbital after the first hydrogenation step, indicating that N atoms interact with  $^*\text{H}$  to generate NRR

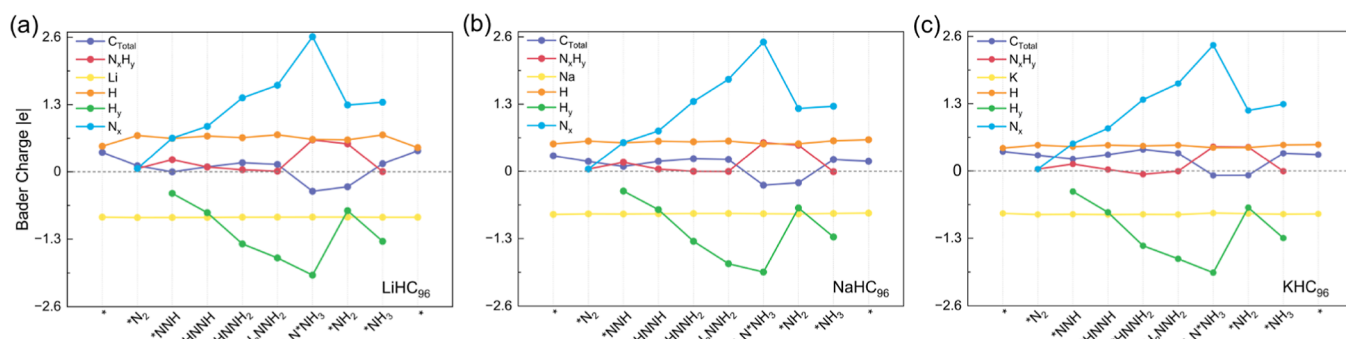


**Figure 6.** Bader charge analysis of the alternative reaction pathway of NRR in the MHC<sub>96</sub> catalysts of (a) LiHC<sub>96</sub>, (b) NaHC<sub>96</sub>, and (c) KHC<sub>96</sub>.

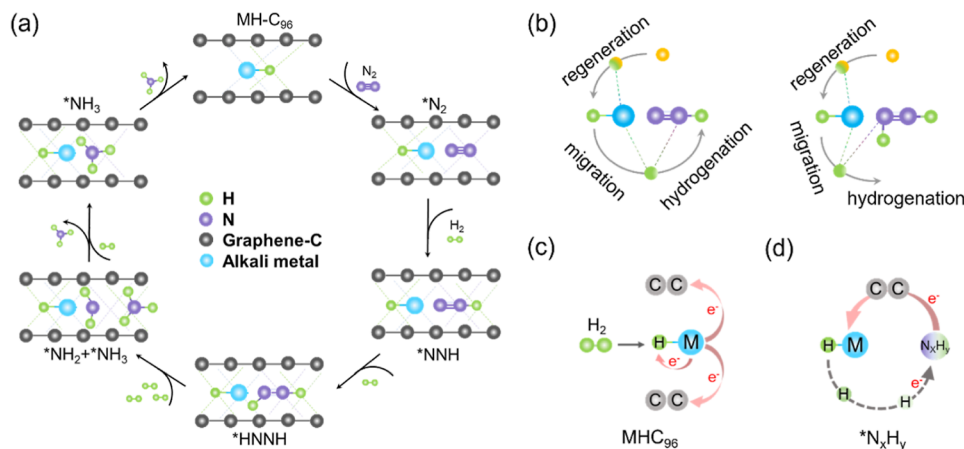


**Figure 7.** (a) Alternative reaction pathway of NRR in the MHC<sub>96</sub> catalyst. The H atom is in green. Graphene is in gray. The nitrogen atom is in purple. The alkali metal atom is in blue. (b) Formation of intermediates and regeneration of the MHC<sub>96</sub> catalyst during the nitrogen reduction process. The key process of electron transfer between graphene, alkali metal hydride, and reaction intermediates, including (c) regeneration of MH-intercalated graphene catalyst, and (d) hydrogenation reaction of nitrogen-based intermediates.

intermediates. The results explain the lower adsorption energies and the higher reaction barriers of N<sub>2</sub> hydrogenation in KHC<sub>96</sub>, as illustrated in Figure 3.

**3.3. Electron Transfer in MHC<sub>96</sub> Catalysts.** The charge state of MHC<sub>96</sub> catalysts affects the catalytic performance of the catalyst. We analyzed the differential charge density to depict the electron distribution between MHC<sub>96</sub> catalysts and the NRR intermediates and the electron transfer between the intermediates and the graphene layers (Figures S13–S17). As shown in Figure 5, the blue region represents electron-deficient areas, and the yellow region represents electron-rich areas. The red line indicates the variation of differential charge density perpendicular to the graphene layer, indicating an overall electron transfer from the alkali metal hydride toward the two adjacent graphene layers, where positive values refer to the gain of electrons and negative values refer to the loss of electron. With the formation of the MHC<sub>96</sub> system, electrons in the alkali metal hydride transfer from the alkali metal to the H atom. The graphene C atoms near the alkali metal exhibit an electron-rich state, while those near the H atom display an electron-deficient state. Specifically, in the LiHC<sub>96</sub> system (Figure 5a–c), as N<sub>2</sub> is adsorbed and the first hydrogenation step takes place, the graphene layers change from an electron-rich state to an electron-deficient state. The interaction between the LiH and the reaction intermediates is more dominant than those with the graphene layers. In the NaHC<sub>96</sub> system (Figure 5d–f), we find that the electron distribution is more uniform along the z-direction compared to the LiHC<sub>96</sub>

and KHC<sub>96</sub> systems, and the alkali metal hydride has the least driving force for electron transfer and the weakest interaction with the graphene layers. In the KHC<sub>96</sub> system (Figure 5g–i), the graphene layers remain in an electron-rich state, while the assembly of N<sub>2</sub> and KH is in an electron-deficient state, indicating a strong interaction between KH and the graphene layers.

We then analyzed the changes of Bader charge of the reaction intermediates in the alternating associative pathway on the MHC<sub>96</sub> catalysts of LiHC<sub>96</sub>, NaHC<sub>96</sub>, and KHC<sub>96</sub> (Figures 6 and S2–S6). When the system of alkali metal hydride-intercalated graphene is formed, the alkali metal loses electrons, and the electron transfer occurs between the activated hydrogen and the graphene layers. The change of Bader charge of N<sub>2</sub> (distal) and N<sub>1</sub> (proximal) is small (Table S7) because there is a strong interaction between the N atoms, and electrons are transferred and dissipated between them as shown in Figure 5. As plotted in Figure 6, within reaction intermediates, it exists a direct relationship between the number of electrons gained by xN atoms (N<sub>x</sub>) and the number of electrons lost by yH atoms (H<sub>y</sub>), indicating the formation of an N–H bond and N atoms receive electrons from the activated H atoms during the NRR process. N<sub>2</sub> (distal) and N<sub>1</sub> (proximal) are the nitrogen atoms which are defined by the distance from the alkali atom. For example, in the first hydrogenation step, the Bader charge of N<sub>2</sub> is from 0.04 |e| to 0.32 |e|, while the number of electrons on H is −0.42 |e| on LiHC<sub>96</sub>, which also happens on NaHC<sub>96</sub> (N<sub>2</sub>: 0.05 |e| → 0.34 |e|

el, H:  $-0.37$  lel) and  $\text{KHC}_{96}$  ( $\text{N}_2$ :  $-0.08$  lel  $\rightarrow$   $0.38$  lel, H:  $-0.38$  lel) (Table S7). The first free  $\text{NH}_3$  is formed when N–N completely breaks, the electrons shared between N1 and N2 disappear, N1 gets electrons from the graphene layers, maintaining the electron balance of the intermediate  $^*\text{NH}_2$ . From  $^*\text{NH}_2$  to  $^*\text{NH}_3$ , N1 gets electrons from  $^*\text{H}$  to form  $^*\text{NH}_3$ , breaking the previous equilibrium of electron formation from the graphene layers, and excess electrons return to the graphene layers. It is also found that the Bader charge of H and alkali metal in the alkali metal hydride remains unchanged, and there exists a charge transfer between the graphene layers ( $C_{\text{Total}}$ ) and the reaction intermediates ( $\text{N}_x\text{H}_y$ ) and an electron redistribution in the intermediates (Figures 6 and S18); thus, the alkali metal hydrides serve as the active center that remains unchanged before and after the hydrogenation reaction. The electron differences between  $C_{\text{Total}}$  and  $^*\text{N}_2$  are  $0.06$  lel ( $\text{LiHC}_{96}$ ,  $\Delta E_{\text{N}_2} = 0.20$  eV),  $0.14$  lel ( $\text{NaHC}_{96}$ ,  $\Delta E_{\text{N}_2} = -0.17$  eV), and  $0.26$  lel ( $\text{KHC}_{96}$ ,  $\Delta E_{\text{N}_2} = -0.24$  eV). The more electron transfer between the graphene layers and  $^*\text{N}_2$ , the lower the  $\text{N}_2$  adsorption energy, making it easier for to be absorbed. The electron differences of  $C_{\text{Total}}$  and the intermediate  $^*\text{NNH}$  are  $0.24$  lel ( $\text{LiHC}_{96}$ ,  $\Delta E_{^*\text{NNH}} = 1.84$  eV),  $0.09$  lel ( $\text{NaHC}_{96}$ ,  $\Delta E_{^*\text{NNH}} = 1.93$  eV), and  $0.09$  lel ( $\text{KHC}_{96}$ ,  $\Delta E_{^*\text{NNH}} = 1.96$  eV). The electron transfer between the graphene layers and the intermediate  $^*\text{NNH}$  is positively correlated with the energy barrier of the first hydrogenation step. Therefore, selecting better alkali metal hydrides to enhance the electron transfer between reaction intermediates and graphene layers will promote the NRR process.

#### 4. DISCUSSION

Based on these results, we further present a schematic description of the NRR process in the  $\text{MHC}_{96}$  catalysts to understand the hydrogenation and electron transfer (Figure 7a). The alkali metal hydride exists stably in the interlayer spacing between the graphene layers to form an MH-intercalated graphene catalyst. After introducing the reactants  $\text{N}_2$  and  $\text{H}_2$ ,  $\text{N}_2$  is adsorbed on the alkali metal inside the catalyst and the activated  $^*\text{H}$  from the alkali metal hydrides attacks the distal N atom to form the  $^*\text{NNH}$  intermediate. Simultaneously,  $\text{H}_2$  is dissociated by attacking the alkali metal to regenerate the alkali metal hydrides, which maintains the catalytic activity of the catalyst (Figure 7b). The second hydrogenation step occurs on the proximal N atom, and the activated  $^*\text{H}$  dissociates from the alkali metal bonds with the proximal N atom to form the  $^*\text{HNNH}$  intermediate. With the alternating associative pathway, the activated  $^*\text{H}$  attacks the two N atoms sequentially until two  $\text{NH}_3$  are generated. Figure 7c shows the electron transfer process in the formation of the MH-intercalated graphene system, where the alkali metal provides electrons to activate the  $\text{H}_2$  and graphene layers to form the  $\text{MHC}_{96}$  system. The dissociated  $^*\text{H}$  gives  $^*\text{N}_2$  the electrons to form the N–H bond (Figure 7d), during which excess electrons are transferred back to the alkali metal through the graphene layers to facilitate the reaction between the alkali metal and the external  $\text{H}_2$ , thus achieving the regeneration of the  $\text{MHC}_{96}$  catalyst.

#### 5. CONCLUSIONS

In this work, we use DFT calculations to explore the catalytic mechanism of NRR on MH-intercalated graphene ( $\text{MHC}_{96}$ ) catalysts. The energy barriers and reaction pathways analysis

revealed that the NRR on these catalysts prefers the alternating associative mechanism. The density of states confirms the direct interaction between alkali metal hydrides and graphene layers and between the nitrogen-based intermediate and graphene layers, respectively. The electron properties were analyzed through the differential charge density and the Bader charge, which showed that the electron transfer pattern in the NRR process is consistent among the three catalysts. The activated  $^*\text{H}$  from the dissociation of alkali metal hydrides contributes to the hydrogenation of  $\text{N}_2$ , and the graphene layers with Å-level confined spacing serve as an electron-transfer medium between the alkali metal hydride and the reaction intermediates, allowing for the regeneration of the  $\text{MHC}_{96}$  catalytic system. Our work provides microscopic insights into the NRR process in MH-intercalated graphene catalysts and some guidance for the design of low-cost and environmentally friendly catalysts.

#### ■ ASSOCIATED CONTENT

##### SI Supporting Information

The Supporting Information is available free of charge at <https://pubs.acs.org/doi/10.1021/acs.energyfuels.4c01071>.

Additional materials and calculation details, including optimized structures, free energy diagrams, orbital data, and charge analysis (PDF)

#### ■ AUTHOR INFORMATION

##### Corresponding Authors

**Haolan Tao** – State Key Laboratory of Chemical Engineering, Shanghai Engineering Research Center of Hierarchical Nanomaterials, School of Chemical Engineering, East China University of Science and Technology, Shanghai 200237, China; School of Chemistry and Molecular Engineering, East China University of Science and Technology, Shanghai 200237, China; Email: [haolan\\_tao@ecust.edu.cn](mailto:haolan_tao@ecust.edu.cn)

**Cheng Lian** – State Key Laboratory of Chemical Engineering, Shanghai Engineering Research Center of Hierarchical Nanomaterials, School of Chemical Engineering, East China University of Science and Technology, Shanghai 200237, China; School of Chemistry and Molecular Engineering, East China University of Science and Technology, Shanghai 200237, China; [orcid.org/0000-0002-9016-832X](https://orcid.org/0000-0002-9016-832X); Email: [lian Cheng@ecust.edu.cn](mailto:lian Cheng@ecust.edu.cn)

##### Authors

**Meng Zhu** – State Key Laboratory of Chemical Engineering, Shanghai Engineering Research Center of Hierarchical Nanomaterials, School of Chemical Engineering, East China University of Science and Technology, Shanghai 200237, China

**Honglai Liu** – State Key Laboratory of Chemical Engineering, Shanghai Engineering Research Center of Hierarchical Nanomaterials, School of Chemical Engineering, East China University of Science and Technology, Shanghai 200237, China; School of Chemistry and Molecular Engineering, East China University of Science and Technology, Shanghai 200237, China; [orcid.org/0000-0002-5682-2295](https://orcid.org/0000-0002-5682-2295)

Complete contact information is available at:

<https://pubs.acs.org/doi/10.1021/acs.energyfuels.4c01071>

##### Notes

The authors declare no competing financial interest.

## ACKNOWLEDGMENTS

This work is sponsored by the National Key R&D Program of China (2022YFB4602101), the Fundamental Research Funds for the Central Universities (2022ZJFH004 and 2024SMECP05), the National Natural Science Foundation of China (Nos. 22278127 and 22378112), the Shanghai Pilot Program for Basic Research (22T01400100-18), and the Postdoctoral Fellowship Program of CPSF (GZC20230801).

## REFERENCES

- (1) Service, R. F. New recipe produces ammonia from air, water, and sunlight. *Science* **2014**, *345* (6197), 610.
- (2) Valera-Medina, A.; Xiao, H.; Owen-Jones, M.; David, W. I. F.; Bowen, P. J. Ammonia for power. *Prog. Energy Combust. Sci.* **2018**, *69*, 63–102.
- (3) Foster, S. L.; Bakovic, S. I. P.; Duda, R. D.; Maheshwari, S.; Milton, R. D.; Minter, S. D.; Janik, M. J.; Renner, J. N.; Greenlee, L. F. Catalysts for nitrogen reduction to ammonia. *Nat. Catal.* **2018**, *1* (7), 490–500.
- (4) Yang, X.; Mukherjee, S.; O'Carroll, T.; Hou, Y.; Singh, M. R.; Gauthier, J. A.; Wu, G. Achievements, challenges, and perspectives on nitrogen electrochemistry for carbon-neutral energy technologies. *Angew. Chem., Int. Ed.* **2023**, *62* (10), No. e202215938.
- (5) Fang, H.; Wu, S.; Ayvali, T.; Zheng, J.; Fellowes, J.; Ho, P.-L.; Leung, K. C.; Large, A.; Held, G.; Kato, R.; Suenaga, K.; Reyes, Y. I. A.; Thang, H. V.; Chen, H.-Y. T.; Tsang, S. C. E. Dispersed surface Ru ensembles on MgO(111) for catalytic ammonia decomposition. *Nat. Commun.* **2023**, *14* (1), 647.
- (6) Makepeace, J. W.; He, T.; Weidenthaler, C.; Jensen, T. R.; Chang, F.; Vegge, T.; Ngene, P.; Kojima, Y.; de Jongh, P. E.; Chen, P.; David, W. I. F. Reversible ammonia-based and liquid organic hydrogen carriers for high-density hydrogen storage: Recent progress. *Int. J. Hydrogen Energy* **2019**, *44* (15), 7746–7767.
- (7) Chang, F.; Guan, Y.; Chang, X.; Guo, J.; Wang, P.; Gao, W.; Wu, G.; Zheng, J.; Li, X.; Chen, P. Alkali and alkaline earth hydrides-driven N<sub>2</sub> activation and transformation over Mn nitride catalyst. *J. Am. Chem. Soc.* **2018**, *140* (44), 14799–14806.
- (8) Wang, P.; Chang, F.; Gao, W.; Guo, J.; Wu, G.; He, T.; Chen, P. Breaking scaling relations to achieve low-temperature ammonia synthesis through LiH-mediated nitrogen transfer and hydrogenation. *Nat. Chem.* **2017**, *9* (1), 64–70.
- (9) Guan, Y.; Liu, C.; Wang, Q.; Gao, W.; Hansen, H. A.; Guo, J.; Vegge, T.; Chen, P. Transition-metal-free barium hydride mediates dinitrogen fixation and ammonia synthesis. *Angew. Chem., Int. Ed.* **2022**, *61* (39), No. e202205805.
- (10) Cao, Y.; Toshcheva, E.; Almaksoud, W.; Ahmad, R.; Tsumori, T.; Rai, R.; Tang, Y.; Cavallo, L.; Kageyama, H.; Kobayashi, Y. Ammonia synthesis via an associative mechanism on alkaline earth metal sites of Ca<sub>3</sub>CrN<sub>3</sub>H. *ChemSusChem* **2023**, *16*, No. e202300234.
- (11) Wu, H.; Yang, L.; Wen, J.; Xu, Y.; Cai, Y.; Gao, W.; Wang, Q.; Guan, Y.; Feng, S.; Cao, H.; He, T.; Liu, L.; Zhang, S.; Guo, J.; Chen, P. Plasma-driven nitrogen fixation on sodium hydride. *Adv. Energy Mater.* **2023**, *13* (27), 2300722.
- (12) Wang, P.; Xie, H.; Guo, J.; Zhao, Z.; Kong, X.; Gao, W.; Chang, F.; He, T.; Wu, G.; Chen, M.; Jiang, L.; Chen, P. The formation of surface lithium-iron ternary hydride and its function on catalytic ammonia synthesis at low temperatures. *Angew. Chem., Int. Ed.* **2017**, *56* (30), 8716–8720.
- (13) Aika, K.-i. Role of alkali promoter in ammonia synthesis over ruthenium catalysts—Effect on reaction mechanism. *Catal. Today* **2017**, *286*, 14–20.
- (14) Chen, Z.; Ye, Y.; Pan, X.; Bao, X. Potassium promoted ferrocene/graphene for ammonia synthesis. *Chem. Res. Chin. Univ.* **2024**, DOI: 10.1007/s40242-024-4019-3.
- (15) Kalucki, K.; Morawski, A. W. Iron intercalated in graphite as catalysts for ammonia synthesis. *J. Chem. Technol. Biotechnol.* **1990**, *47* (4), 357–363.
- (16) Andersen, S. Z.; Čolić, V.; Yang, S.; Schwalbe, J. A.; Nielander, A. C.; McEnaney, J. M.; Enemark-Rasmussen, K.; Baker, J. G.; Singh, A. R.; Rohr, B. A.; Statt, M. J.; Blair, S. J.; Mezzavilla, S.; Kibsgaard, J.; Vesborg, P. C. K.; Cargnello, M.; Bent, S. F.; Jaramillo, T. F.; Stephens, I. E. L.; Nørskov, J. K.; Chorkendorff, I. A rigorous electrochemical ammonia synthesis protocol with quantitative isotope measurements. *Nature* **2019**, *570* (7762), 504–508.
- (17) Andersen, S. Z.; Statt, M. J.; Bukas, V. J.; Shapel, S. G.; Pedersen, J. B.; Kreml, K.; Saccoccio, M.; Chakraborty, D.; Kibsgaard, J.; Vesborg, P. C. K.; Nørskov, J.; Chorkendorff, I. Increasing stability, efficiency, and fundamental understanding of lithium-mediated electrochemical nitrogen reduction. *Energy Environ. Sci.* **2020**, *13* (11), 4291–4300.
- (18) Li, K.; Andersen, S. Z.; Statt, M. J.; Saccoccio, M.; Bukas, V. J.; Kreml, K.; Sažinas, R.; Pedersen, J. B.; Shadravan, V.; Zhou, Y.; Chakraborty, D.; Kibsgaard, J.; Vesborg, P. C. K.; Nørskov, J. K.; Chorkendorff, I. Enhancement of lithium-mediated ammonia synthesis by addition of oxygen. *Science* **2021**, *374* (6575), 1593–1597.
- (19) Suryanto, B. H. R.; Matuszek, K.; Choi, J.; Hodgetts, R. Y.; Du, H.-L.; Bakker, J. M.; Kang, C. S. M.; Cherepanov, P. V.; Simonov, A. N.; MacFarlane, D. R. Nitrogen reduction to ammonia at high efficiency and rates based on a phosphonium proton shuttle. *Science* **2021**, *372* (6547), 1187–1191.
- (20) Fu, X.; Xu, A.; Pedersen, J. B.; Li, S.; Sažinas, R.; Zhou, Y.; Andersen, S. Z.; Saccoccio, M.; Deissler, N. H.; Mygind, J. B. V.; Kibsgaard, J.; Vesborg, P. C. K.; Nørskov, J. K.; Chorkendorff, I. Phenol as proton shuttle and buffer for lithium-mediated ammonia electrosynthesis. *Nat. Commun.* **2024**, *15* (1), 2417.
- (21) Li, K.; Shapel, S. G.; Hochfilzer, D.; Pedersen, J. B.; Kreml, K.; Andersen, S. Z.; Sažinas, R.; Saccoccio, M.; Li, S.; Chakraborty, D.; Kibsgaard, J.; Vesborg, P. C. K.; Nørskov, J. K.; Chorkendorff, I. Increasing current density of Li-mediated ammonia synthesis with high surface area copper electrodes. *ACS Energy Lett.* **2022**, *7* (1), 36–41.
- (22) Li, S.; Zhou, Y.; Li, K.; Saccoccio, M.; Sažinas, R.; Andersen, S. Z.; Pedersen, J. B.; Fu, X.; Shadravan, V.; Chakraborty, D.; Kibsgaard, J.; Vesborg, P. C. K.; Nørskov, J. K.; Chorkendorff, I. Electrosynthesis of ammonia with high selectivity and high rates via engineering of the solid-electrolyte interphase. *Joule* **2022**, *6* (9), 2083–2101.
- (23) Du, H.-L.; Chatti, M.; Hodgetts, R. Y.; Cherepanov, P. V.; Nguyen, C. K.; Matuszek, K.; MacFarlane, D. R.; Simonov, A. N. Electroreduction of nitrogen with almost 100% current-to-ammonia efficiency. *Nature* **2022**, *609* (7928), 722–727.
- (24) Fu, X.; Pedersen, J. B.; Zhou, Y.; Saccoccio, M.; Li, S.; Sažinas, R.; Li, K.; Andersen, S. Z.; Xu, A.; Deissler, N. H.; Mygind, J. B. V.; Wei, C.; Kibsgaard, J.; Vesborg, P. C. K.; Nørskov, J. K.; Chorkendorff, I. Continuous-flow electrosynthesis of ammonia by nitrogen reduction and hydrogen oxidation. *Science* **2023**, *379* (6633), 707–712.
- (25) Fu, X.; Niemann, V. A.; Zhou, Y.; Li, S.; Zhang, K.; Pedersen, J. B.; Saccoccio, M.; Andersen, S. Z.; Enemark-Rasmussen, K.; Benedek, P.; Xu, A.; Deissler, N. H.; Mygind, J. B. V.; Nielander, A. C.; Kibsgaard, J.; Vesborg, P. C. K.; Nørskov, J. K.; Jaramillo, T. F.; Chorkendorff, I. Calcium-mediated nitrogen reduction for electrochemical ammonia synthesis. *Nat. Mater.* **2024**, *23* (1), 101–107.
- (26) Comanescu, C. Graphene Supports for Metal Hydride and Energy Storage Applications. *Crystals* **2023**, *13* (6), 878.
- (27) Bramwell, P. L.; Gao, J.; de Waal, B.; de Jong, K. P.; Klein Gebbink, R. J. M.; de Jongh, P. E. A transition-metal-free hydrogenation catalyst: Pore-confined sodium Alanate for the hydrogenation of alkynes and alkenes. *J. Catal.* **2016**, *344*, 129–135.
- (28) Enoki, T.; Miyajima, S.; Sano, M.; Inokuchi, H. Hydrogen-alkali-metal-graphite ternary intercalation compounds. *J. Mater. Res.* **1990**, *5* (2), 435–466.
- (29) Morawski, A. W. Application of CoC<sub>12</sub>-K-graphite intercalation compounds. *Synth. Met.* **1993**, *59*, 249–252.
- (30) Comanescu, C. Recent Development in Nanoconfined Hydrides for Energy Storage. *Int. J. Mol. Sci.* **2022**, *23* (13), 7111.

- (31) Sreedhar, I.; Kamani, K. M.; Kamani, B. M.; Reddy, B. M.; Venugopal, A. A Bird's Eye view on process and engineering aspects of hydrogen storage. *Renew. Sustain. Energy Rev.* **2018**, *91*, 838–860.
- (32) Ohta, T.; Bostwick, A.; Seyller, T.; Horn, K.; Rotenberg, E. Controlling the electronic structure of bilayer graphene. *Science* **2006**, *313*, 951–954.
- (33) Varykhalov, A.; Sánchez-Barriga, J.; Marchenko, D.; Hlawenka, P.; Mandal, P. S.; Rader, O. Tunable Fermi level and hedgehog spin texture in gapped graphene. *Nat. Commun.* **2015**, *6* (1), 7610.
- (34) Halle, J.; Néel, N.; Fonin, M.; Brandbyge, M.; Kröger, J. Understanding and engineering phonon-mediated tunneling into graphene on metal surfaces. *Nano Lett.* **2018**, *18* (9), 5697–5701.
- (35) N'Diaye, A. T.; Coraux, J.; Plasa, T. N.; Busse, C.; Michely, T. Structure of epitaxial graphene on Ir(111). *New J. Phys.* **2008**, *10*, 043033.
- (36) Silva, C. C.; Cai, J.; Jolie, W.; Dombrowski, D.; Farwick zum Hagen, F. H.; Martínez-Galera, A. J.; Schlueter, C.; Lee, T.-L.; Busse, C. Lifting epitaxial graphene by intercalation of alkali metals. *J. Phys. Chem. C* **2019**, *123* (22), 13712–13719.
- (37) Ahmad, S.; Miró, P.; Audiffred, M.; Heine, T. Tuning the electronic structure of graphene through alkali metal and halogen atom intercalation. *Solid State Commun.* **2018**, *272*, 22–27.
- (38) Shi, M.; Zhang, W.; Li, Y.; Chu, Y.; Ma, C. a. Tungsten carbide-reduced graphene oxide intercalation compound as co-catalyst for methanol oxidation. *Chin. J. Catal.* **2016**, *37* (11), 1851–1859.
- (39) Kikuchi, E.; Ino, T.; Morita, Y. Catalytic synthesis of hydrocarbons from carbon monoxide and hydrogen on lamellar compound of graphite intercalated by ferric chloride. *J. Catal.* **1979**, *57* (1), 27–34.
- (40) Durajski, A. P.; Skoczylas, K. M.; Szczęśniak, R. Superconductivity in bilayer graphene intercalated with alkali and alkaline earth metals. *Phys. Chem. Chem. Phys.* **2019**, *21* (11), 5925–5931.
- (41) Kaneko, T.; Saito, R. First-principles study on interlayer state in alkali and alkaline earth metal atoms intercalated bilayer graphene. *Surf. Sci.* **2017**, *665*, 1–9.
- (42) Chang, F.; Tezsevin, I.; de Rijk, J. W.; Meeldijk, J. D.; Hofmann, J. P.; Er, S.; Ngene, P.; de Jongh, P. E. Potassium hydride-intercalated graphite as an efficient heterogeneous catalyst for ammonia synthesis. *Nat. Catal.* **2022**, *5* (3), 222–230.
- (43) Kresse, G.; Hafner, J. Ab initio molecular dynamics for open-shell transition metals. *Phys. Rev. B: Condens. Matter Mater. Phys.* **1993**, *48* (17), 13115–13118.
- (44) Kresse, G.; Furthmüller, J. Efficient iterative schemes for ab initio total-energy calculations using a plane-wave basis set. *Phys. Rev. B: Condens. Matter Mater. Phys.* **1996**, *54* (16), 11169–11186.
- (45) Kresse, G.; Furthmüller, J. Efficiency of ab-initio total energy calculations for metals and semiconductors using a plane-wave basis set. *Comput. Mater. Sci.* **1996**, *6* (1), 15–50.
- (46) Perdew, J. P.; Burke, K.; Ernzerhof, M. Generalized Gradient Approximation Made Simple. *Phys. Rev. Lett.* **1996**, *77* (18), 3865–3868.
- (47) Blöchl, P. E. Projector augmented-wave method. *Phys. Rev. B: Condens. Matter Mater. Phys.* **1994**, *50* (24), 17953–17979.
- (48) Grimme, S.; Antony, J.; Ehrlich, S.; Krieg, H. A consistent and accurate ab initio parametrization of density functional dispersion correction (DFT-D) for the 94 elements H-Pu. *J. Chem. Phys.* **2010**, *132* (15), 154104.
- (49) Zheng, J.; Liao, F.; Wu, S.; Jones, G.; Chen, T.-Y.; Fellowes, J.; Sudmeier, T.; McPherson, I. J.; Wilkinson, I.; Tsang, S. C. E. Efficient non-dissociative activation of dinitrogen to ammonia over lithium-promoted ruthenium nanoparticles at low pressure. *Angew. Chem., Int. Ed.* **2019**, *58* (48), 17335–17341.
- (50) Wang, X.; Peng, X.; Chen, W.; Liu, G.; Zheng, A.; Zheng, L.; Ni, J.; Au, C.-t.; Jiang, L. Insight into dynamic and steady-state active sites for nitrogen activation to ammonia by cobalt-based catalyst. *Nat. Commun.* **2020**, *11* (1), 653.
- (51) Kobayashi, Y.; Tang, Y.; Kageyama, T.; Yamashita, H.; Masuda, N.; Hosokawa, S.; Kageyama, H. Titanium-Based Hydrides as heterogeneous catalysts for ammonia synthesis. *J. Am. Chem. Soc.* **2017**, *139* (50), 18240–18246.
- (52) Ertl, G.; Thiele, N. XPS studies with ammonia synthesis catalysts. *Appl. Surf. Sci.* **1979**, *3* (1), 99–112.
- (53) Liu, C.; Wang, Q.; Guo, J.; Vegge, T.; Chen, P.; Hansen, H. A. Formation of a complex active center by Ba<sub>2</sub>RuH<sub>6</sub> for nondissociative dinitrogen activation and ammonia formation. *ACS Catal.* **2022**, *12* (7), 4194–4202.
- (54) Rösch, B.; Gentner, T. X.; Langer, J.; Färber, C.; Eysel, J.; Zhao, L.; Ding, C.; Frenking, G.; Harder, S. Dinitrogen complexation and reduction at low-valent calcium. *Science* **2021**, *371* (6534), 1125–1128.